# Spin-Orbit Modal Optical Vortex Beam Shaping from Dielectric Metasurfaces

Mingke Jin, Benjamin Sanchez-Padilla, Xuan Liu, Yutao Tang, Zixian Hu, Kingfai Li, Delphine Coursault, Guixin Li, Etienne Brasselet

# Spin-Orbit Modal Optical Vortex Beam Shaping from Dielectric Metasurfaces

*Mingke Jin, Benjamin Sanchez-Padilla, Xuan Liu, Yutao Tang, Zixian Hu, Kingfai Li, Delphine Coursault, Guixin Li,* and Etienne Brasselet**

**Optical information and communication technologies are essentially based on the ability to shape the light field, either at the transmission or at the reception of the optical signal. Nowadays, wavelength and polarization state are already implemented in current telecom architectures and adding the spatial structuring of the light field as a novel degree of freedom to enhance data rate is desirable. In this context, the development of optical devices to shape optical modes belonging to orthogonal basis remains challenging. Here, in the context of singular optics, this work reports on the design, fabrication, and characterization of modal optical vortex beam shaping of paraxial light in the visible domain, in the framework of the Laguerre–Gauss basis. Both the azimuthal and radial degrees of freedom are univocally shaped via optical spin-orbit interaction mediated by dielectric metasurfaces by combining the spatial modulation of amplitude, geometric phase, and dynamic phase. These results not only demonstrate the realization of new optical components, but also highlight how metasurface-based technologies can contribute to optical information processing in the classical or quantum regime.**

## 1. Introduction

Optical modes and structured light are intimately related since the advent of lasers. Indeed, we can now recognize in earlier works in the 1960s on optical resonators the emergence of optical vortex modes associated with on-axis optical phase singularities and ensuing doughnut shaped intensity patterns.[1] The underlying helical-shaped equiphase surfaces for the light field remained barely studied for almost three decades, though the fabrication of helical phase plates[2] and the interferometric assessment of beams with helical phase profile[3] date back to the 1970s. Optical waves rotating around a phase singularity has only been articulated in the late 1980s.[4] Soon after, within a paraxial wave optics framework, Laguerre–Gauss beams have been recognized as a basis made out of optical vortex modes carrying an integer multiple of $\hbar$ of optical orbital angular momentum per photon,[5] which kick-started a wealth of fundamental and technological developments that are still ongoing. The generation of Laguerre–Gauss beams involves the shaping of azimuthal and radial degrees of freedom (respectively labeled by the indices $l \in \mathbb{Z}$ and $p \in \mathbb{N}$)-according to the paraxial expression of the electric field in the cylindrical coordinate system $(r, \phi, z)$[6]

$$E_{l,p}(r,\phi,z;w_0) \propto \frac{w_0}{w(z)}\left[\frac{r}{w(z)}\right]^{|l|} L_p^{|l|}\left(\frac{2r^2}{w(z)^2}\right)\times\exp\left[-\frac{r^2}{w(z)^2}\right] \times\exp\left\{i\left[\frac{k_0 r^2 z}{2\left(z^2+z_0^2\right)}+l\phi-\left(2p+|l|+1\right)\arctan\left(\frac{z}{z_0}\right)\right]\right\} \quad (1)$$

for a beam propagating toward $z > 0$. There, $L_p^{|l|}(x)=\sum_{m=0}^{p}\frac{(|l|+p)!}{(|l|+m)!(p-m)!m!}(-x)^m$ with $x = 2r^2/w(z)^2$, $w(z)=w_0\sqrt{1+(z/z_0)^2}$, $w_0$ the beam waist radius, $z_0 = k_0 w_0^2/2$ the Rayleigh distance, $k_0 = 2\pi/\lambda$ the wavevector in the free space and $\lambda$ the wavelength. Note that the free-space propagation factor $\exp(-i\omega t + ik_0 z)$ has been omitted in Equation (1).

Among the different strategies developed so far to form a Laguerre–Gauss $(l, p)$ mode from a fundamental Gaussian beam, the digital approach based on spatial light modulators appears to be the most flexible to date.[7] However, the implementation of this approach requires an experimental setup

M. Jin, X. Liu, Y. Tang, Z. Hu, K. Li, G. Li
Department of Materials Science and Engineering
Southern University of Science and Technology
Shenzhen 518055, P. R. China
E-mail: ligx@sustech.edu.cn
B. Sanchez-Padilla, D. Coursault, E. Brasselet
Laboratoire Ondes et Matière d'Aquitaine
CNRS
University of Bordeaux
Talence F-33400, France
E-mail: etienne.brasselet@u-bordeaux.fr
X. Liu
Institute of Laser Engineering
Faculty of Materials and Manufacturing
Beijing University of Technology
Beijing 100124, P. R. China
G. Li
Shenzhen Institute for Quantum Science and Engineering
Southern University of Science and Technology
Shenzhen 518055, P. R. China

around the modulator and knowhow to mitigate the aberrations inherent to the optical system. This limits their use to expert users and calls for the development of the modal counterpart of single-piece large-aperture on-axis optical devices imparting azimuthally varying phase profile to an incident beam, which is the purpose of the present work.

Optical elements characterized by a pure phase transmittance of the form $t \propto \exp(il\phi)$ remain often approximated as Laguerre–Gaussian beam generators for the indices $(l, 0)$ whereas it is now well-established that they inherently produce coherent superposition of radial modes.[8] In fact, in the absence of an optical vortex mask combining amplitude and phase mod-ulation, a pure Laguerre–Gaussian mode cannot be conveni-ently extracted from the total field emerging from a single-piece optical vortex mask. Nevertheless, the latter nonmodal vortex masks, now brought to the level of commercial devices during the last decade owing to the development of several micro/nanofabrication technologies and optical materials—one can mention strategies based on photopatterned liquid crystals or liquid crystal polymers, nanostructured glasses, carved crystals, and 3D printed photoresists—have contributed decisively to the progress of the research field dealing with structured light. For this reason, it is likely that the advent of simple, robust, and efficient modal vortex beam generators will open novel perspectives.

It should be noted that although efforts to incorporate "$p$ add-on" to "$l$ only" single-piece user-friendly optical elements began some time ago with the incorporation of $\pi$-phase jumps along the radial coordinate,[9–11] the design and fabrication of optical masks operating with complex amplitude modulation remains a current challenge. Recently, the optical spin-orbit interaction occurring when light propagates in inhomogeneous anisotropic media has been theoretically identified as a tool for modal beam shaping where a prescribed modal information is selectively associated to a given uniform polarization state and which can therefore be extracted with the use of standard polarization optics components.[12] The proposal can be described in a generic manner by considering a planar optical element lying in the $(x, y)$ plane and whose effective behavior can be described as that of space-variant lossless anisotropic wave-plate characterized by its anisotropic retardance $\delta = \frac{(\Phi_{\parallel} - \Phi_{\perp})}{k_0}$, where $\Phi_{\parallel}$ [$\Phi_{\perp}$] is the transmission phase for the electric field component parallel [perpendicular] to the slow-axis, and the in-plane polar orientation angle $\psi$ of its slow-axis. Within a paraxial framework, neglecting the diffraction through the optical element itself as well as refractive reflection, a normally incident circularly polarized beam with helicity $\sigma = \pm 1$ described as $\mathbf{E}_{\text{in}} = E_{\text{in}}\mathbf{c}_{\sigma}$, where $\mathbf{c}_{\sigma} = (\mathbf{x} + i\sigma\mathbf{y})/\sqrt{2}$, emerges as (see Section S1, Supporting Information)

$$\mathbf{E}_{\text{out}} = E_{\text{in}} e^{i\Phi_{\text{d}}} \left[ \cos\left(\frac{\pi\delta}{\lambda}\right)\mathbf{c}_{\sigma} + i \sin\left(\frac{\pi\delta}{\lambda}\right) e^{i\Phi_{\text{g}}} \mathbf{c}_{-\sigma} \right] \tag{2}$$

where $\Phi_{\text{d}} = (\Phi_{\parallel} + \Phi_{\perp})/2$ is the helicity-independent dynamic phase and $\Phi_{\text{g}} = 2\sigma\psi$ is the helicity-dependent geometric phase. The required amplitude and phase control to obtain an output $(l, p)$ mode out of an incident fundamental Gaussian beam $\mathbf{E}_{\text{in}} = E_0 e^{-r^2/w_{\text{in}}^2}\mathbf{c}_{\sigma}$ shaping can thus be obtained by selecting the $\mathbf{c}_{-\sigma}$ polarized component of the output filed provided that[12]

$$\delta_{l,p}(r) = \frac{\lambda}{\pi} \arcsin\left\{ \frac{\left| E_{l,p}(r,0,0;w_{\text{out}}) \right| e^{r^2/w_{\text{in}}^2}}{\max\left[ \left| E_{l,p}(r,0,0;w_{\text{out}}) \right| e^{r^2/w_{\text{in}}^2} \right]} \right\} \tag{3}$$

$$\psi_{l,p}(r,\phi) = \frac{\sigma}{2}\left[ l'\phi - \Phi_{\text{d}}(r) \right] - \frac{\pi}{4}\left\{ 1 - \text{sign}\left[ L_p^{|l|}\left( \frac{2r^2}{w_{\text{in}}^2} \right) \right] \right\} \tag{4}$$

where the output beam waist radius satisfies $w_{\text{out}} < w_{\text{in}}$, which ensures that the denominator of Equation (3) does not diverge, and where the material structuring azimuthal index $l'$ satisfies $l = \sigma l'$.

Such an approach to modal beam shaping based on the spin-orbit interaction of light has been previously investigated experimentally using optically nanostructured silica glass[13,14] or metallic metasurfaces.[15] It has also given rise to recent theoretical discussions.[16,17] However, despite the research field of optical vortex generation by metasurfaces being well-developed,[18] spin-orbit modal optical vortex beam shaping from dielectric metasurfaces has not yet been addressed experimentally and present works fills this gap by choosing the visible domain for the case study that is summarized by the sketch shown in **Figure 1**.

## 2. Results

Here, we restrict our demonstration to the fundamental radial mode $p = 0$, exploring three values for the material structuring

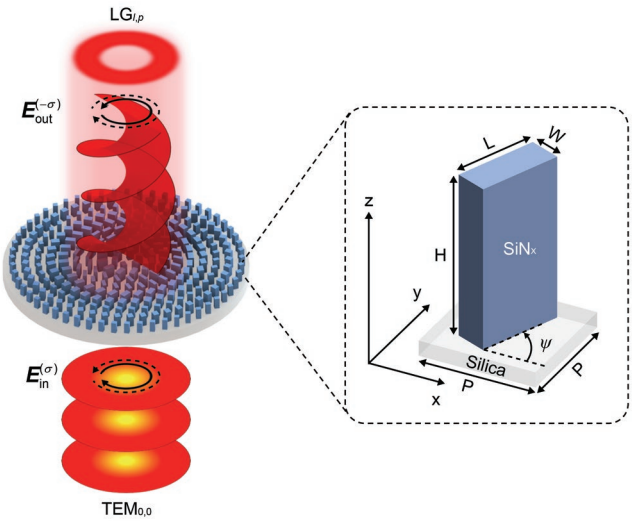


**Figure 1.** Illustration of the spin-orbit generation of a pure Laguerre–Gauss beam of order $(l, p)$ (labeled as LG$_{l,p}$) from an incident circularly polarized fundamental Gaussian beam (labeled as TEM$_{0,0}$) with a dielectric metasurface. Solid and dashed circling arrows refer to electric field temporal rotation in the plane $(x, y)$ for $\sigma = \mp 1$, respectively. Inset: sketch of a meta-atom made of silicon nitride nanopillar of length $L$, width $W$, and height $H$, and having a $P^2$ footprint standing on a silica substrate.

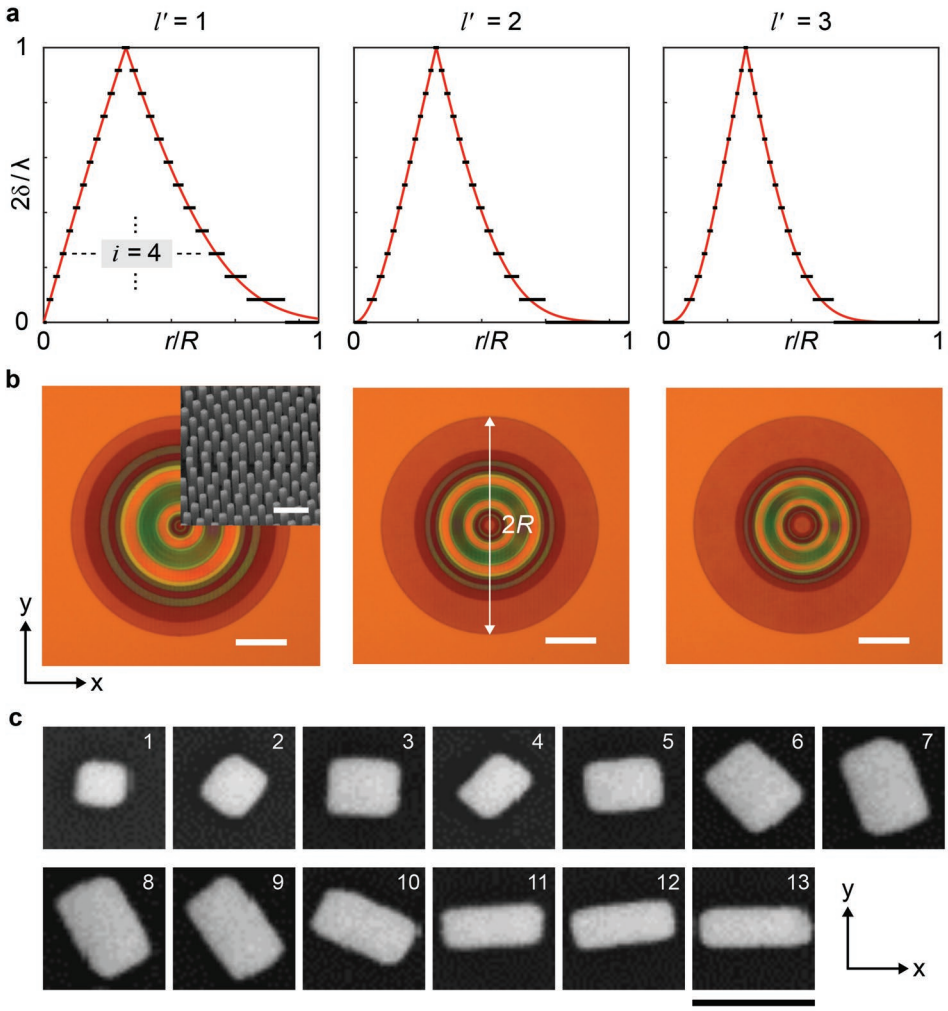


**Figure 2.** a) Red curves: theoretical radial profiles of the retardance given by Equation (5) for $l'$ = (1, 2, 3), $R$ = 215 µm and $w_{design}$ = 91 µm. Black segments: piecewise design according to numerical simulations, see text for details. Except for $i$ = 13 that corresponds to the retardance peak, there are two zones having identical meta-atoms, see the example for $i$ = 4 on the leftmost panel. b) Reflection optical microscope images of the fabricated modal metasurfaces, see Experimental Section for details. Scale bar: 100 µm. Inset: slanted view scanning electron microscope (SEM) image of the central part of the modal metasurface. Scale bar: 1 µm. See also Figure S4a–f (Supporting Information). c) Top view SEM images of the 13 individual meta-atoms associated with increasing retardance from along the $x$ axis ($x > 0$) where the label $i$ = 1 ($\delta = 0$) to $i$ = 13 ($\delta = \lambda/2$), see also Tables S1 and S2 (Supporting Information). Scale bar: $P$ = 430 nm.

azimuthal index $l'$ = 1, 2, 3. Equations (3) and (4) are thus simplified to the following analytical expressions[12]

$$\delta_{l,0}(r) = \frac{\lambda}{\pi}\arcsin\left\{\left(\frac{r\sqrt{2}}{w_{design}}\right)^{|l|}\exp\left[|l|\left(\frac{1}{2}-\frac{r^2}{w_{design}^2}\right)\right]\right\} \quad (5)$$

$$\psi_{l,0}(r,\phi) = \frac{\sigma}{2}\left[l'\phi - \Phi_d(r)\right] \quad (6)$$

where $w_{design}$ is the characteristic radius for the optimal design that maximizes the modal output power fraction when $w_{in} = w_{design}$. This leads to an output waist for the shaped modal beam $w_{out} = w_{design}/\sqrt{1+|l|}$. The radial profile for retardance given by Equation (5) is shown by the red curves in **Figure 2**a.

The experimental demonstration is made with metasurfaces consisting of parallelipedic silicon nitride nanopillars standing on a silica substrate (Figure 2b,c). Each of them are placed at the center of a unit cell with subwavelength footprint of 0.185 µm$^2$ and characterized by their height $H$, cross-section $L \times W$, and orientation polar angle $\psi$ in the ($x$, $y$) plane, as depicted in Figure 1. Nanofabrication constraints impose to work at fixed $H$ while the required design defined by Equations (3) and (4) is met by using space-variant geometrical parameters $L$, $W$, and $\psi$. The latter are determined numerically using the FDTD method by evaluating the magnitude and phase of the contracircular complex electric field transmittance, $t_{-\sigma}$ in the plane of parameters ($L$, $W$). The calculations are made by using the complex refractive index of silicon nitride determined experimentally by spectroscopic ellipsometry of a film with uniform thickness of 1400 nm, namely $n$ = 1.9656 (Section S2, Supporting Information). Simulation results are shown in **Figure 3** for $H$ = 1400 nm, 120 nm ≤ ($L$, $W$) ≤ 370 nm, and operating wavelength $\lambda$ = 633 nm.

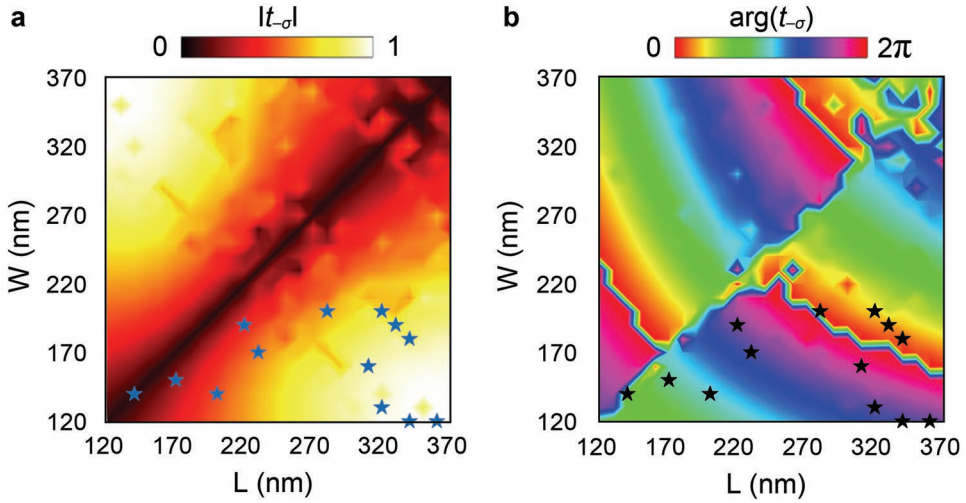


**Figure 3.** Numerical simulations of the magnitude (a) and phase (b) of the complex transmittance $t_{-\sigma}$ associated with the contracircularly polarized electric field contribution to the output field, for $H = 1400$ nm, 120 nm ≤ ($L$, $W$) ≤ 370 nm and operating wavelength $\lambda = 633$ nm. The results are identical for $\sigma = \pm 1$. The selected meta-atoms which are used to fabricate the devices reported in this work are marked with blue (a) and black (b) star markers.

We adopt a concentric design made of $2N - 1$ radial zones from $r = 0$ to $R = 215$ μm associated to a discrete set of $N$ distinct meta-atoms. We choose $w_{\text{design}} \simeq 90$ μm in order to have virtually all the incident power passing through the aperture of the device and a trade-off number of $N = 13$, see Figure 2a,b. The definition of the geometrical parameters $L$, $W$, and $\psi$ of the meta-atoms includes three steps. First, from Equation (2) we have $t_{-\sigma} = i\exp(i\Phi_{\text{d}})\sin(\pi\delta/\lambda)$, both the retardance and the dynamic phase can be formally expressed as a function of $t_{-\sigma}$ according to

$$\delta = \frac{\lambda}{\pi}\arcsin\left(|t_{-\sigma}|\right) \tag{7}$$

$$\Phi_{\text{d}} = \arg(t_{-\sigma}) - \frac{\pi}{2} \tag{8}$$

where we notice that the constant offset in Equation (8) has no influence on the modal design and can thus be taken as an arbitrary value. Second, we define an almost evenly distributed set of values $\delta_{i=1,\ldots,13}$ ranging from 0 to $\lambda/2$ and select the length and width of the meta-atoms according to Equation (7), see star markers in Figure 3a, which allows determining the corresponding dynamic phase is obtained from Figure 3b and Equation (8). Third, the orientation of the meta-atom is subsequently obtained from Equation (6). The detailed geometrical parameters of the meta-atoms are given in Table S1 (Supporting Information).

The modal metasurfaces are fabricated using electron beam lithography according to a multiple-step protocol described in Experimental Section, and their structural characterization is summarized in Figure 2b,c. On the one hand, the top view optical images in the reflection mode are shown in Figure 2b, which allow identifying the 25 radial zones for each device, where different values of retardance are qualitatively retrieved from visual inspection as distinct colors. On the other hand, the top view scanning electron microscope (SEM) images of each of the 13 individual meta-atoms along the $x$ axis allow validating their prescribed cross-section in the plane ($x$, $y$) and orientation taken as $\psi = [\arg(t_{-\sigma}) - \pi/2]/2$, which corresponds to a modal behavior for $\sigma = -1$, hence $l = (-1, -2, -3)$. In what follows, without loss of generality, the fabricated metasurfaces are placed in the course of an incident fundamental Gaussian beam propagating toward $z > 0$ according to Figure 1 and we consequently use $\sigma = -1$.

The experimental validation of the modal beam shaping features of the fabricated metasurfaces is carried out by using a supercontinuum laser source spectrally filtered at $\lambda = 633$ nm by an acousto-optical filter, as sketched in **Figure 4**a. The incident beam is $\mathbf{c}_{\sigma}$-polarized by means of a linear polarizer and a quarter-wave plate and normally incident onto the metasurface placed at the focal plane of a lens, which gives an input beam waist $w_{\text{in}} \simeq 90$ μm at $z = 0$. The transmitted light at a distance $z$ from the metasurface is reimaged by an objective lens and a tube lens together with another quarter-wave plate and linear polarizer to select the $\mathbf{c}_{-\sigma}$ -polarized component of the shaped light beam, whose transverse intensity distribution are recorded by a digital camera. The meridional intensity cross-section in the plane ($y$, $z$) intensity profiles are shown in Figure 4b–d from $z = 0$ to 27 mm for $l' = (1, 2, 3)$, respectively. Correspondingly, the doughnut shaped transverse intensity distribution at $z = 15$ mm are shown in Figure 4e,g,i while the topological charge $l = \sigma l'$ of the vortex mode is assessed by the cylindrical lens imaging at $z = 10$ mm using a cylindrical lens instead of the tube lens, see Figure 4f,h,j where the number and inclination of dark stripes (see white arrows) inform on the absolute value and sign of $l$.[19] These propagation features highlight the generation of Laguerre–Gauss ($l$, 0) modes whose transverse intensity distribution is $z$-independent up to a stretching factor. In addition, these experimental results are supported by numerical simulations of the beam propagation (see Experimental Section) as illustrated in the inset panels of Figure 4.

Noteworthy, the achieved modal characteristics can be also appreciated by comparing these observations with that obtained using standard $l$-only vortex beam shapers for the same

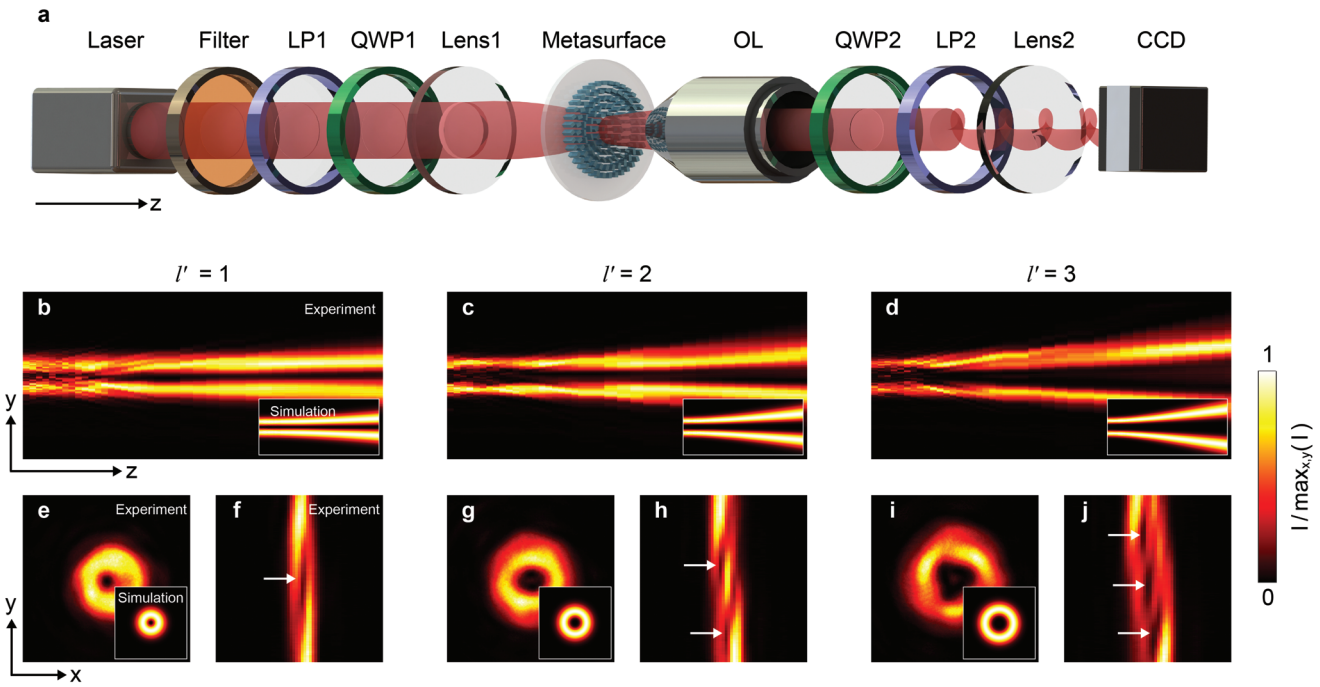


**Figure 4.** a) Experimental setup used for the optical characterization of the modal metasurfaces with $l'$= (1, 2, 3). Filter: spectral filtering of the supercontinuum laser; LP1 and LP2: linear polarizers; QWP1 and QWP2: quarter-wave plates; Lens1: 250 mm focal length; OL: objective lens (10× magnification, NA = 0.25 numerical aperture); Lens2: tube lens with 100 mm effective focal length [all panels except panels (f, h, j)] or cylindrical lens with 75 mm focal length [panels (f, h, j)]; CCD: charge-coupled device used to image the beam. b–d) Experimental meridional ($y$, $z$) intensity cross-section of the shaped $\mathbf{c}_{-\sigma}$-polarized optical mode for $l'$= (1, 2, 3), respectively. The panels refer to –250 µm < $y$ < 250 µm and 0 mm < $z$ < 27 mm. Insets: corresponding simulations. e,g,i) Experimental transverse intensity cross-section at $z$ = 15 mm with -250 µm < ($x$, $y$) < 250 µm. Insets: corresponding simulations. f,h,j) Experimental assessment of the optical vortex carried by the modal beam using the cylindrical lens imaging.

wavelength associated with $\delta = \lambda/2$ whatever $l$ and $\psi_l = (l'/2)\phi$ with $l = \sigma l'$. We have designed, fabricated, and characterized such optical elements for $l'$= (1, 2, 3), see Figures S8 and S9 (Supporting Information). Being nonmodal by nature, these optical vortex shapers lead to the generation of a superposition of radial modes, hence to $z$-dependent transverse intensity profiles.

## 3. Discussion

The need for compensating the space-variant dynamic phase resulting from space-variant from retardance, which is at the heart of the design given by Equation (6) can be appreciated by comparing the two situations $\sigma = \pm 1$ all other things being fixed. Here, $\sigma$ = –1 corresponds to the modal behavior while $\sigma$ = 1 does not. This is illustrated in **Figure 5** where the experimental and simulated beam propagation properties are shown for $l'$= (1, 2, 3). The comparison with Figure 4b–d vividly emphasizes the paramount importance of dynamic phase compensation for spin-orbit photonic devices. Still, by flipping upside down the metasurface one gets a modal behavior for orthogonally incident circular polarization state $\sigma = 1$, hence $l$ = (1, 2, 3), as previously noted in Ref. [12].

Although all the experimental observations validate qualitatively the expected behaviors, we note that the axisymmetry is broken in experiments, as shown in Figures 4 and 5. This mainly comes from technological limitations, recalling that the fabricated subwavelength nanopillars have neither sharp edges (see Figure 2c) nor fully reproducible shapes (see Figure S4g, Supporting Information). Also, adjacent nanopillars are

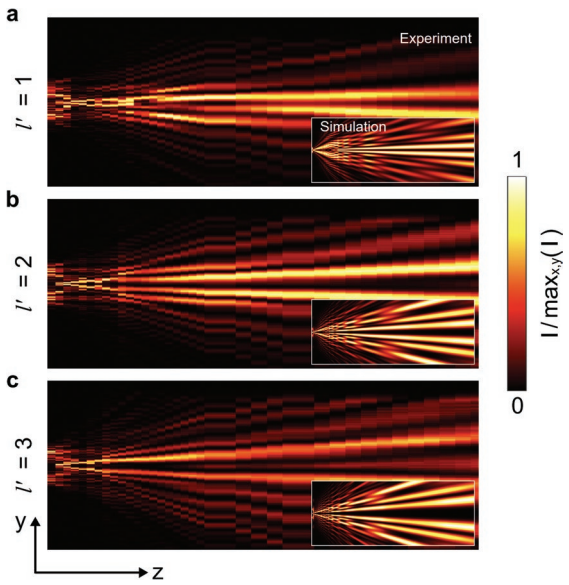


**Figure 5.** Experimental meridional ($y$, $z$) intensity cross-section of the shaped $\mathbf{c}_{\sigma}$-polarized output field for $l'$= (1, 2, 3). The panels refer to –250 µm < $y$ < 250 µm and 0 mm < $z$ < 27 mm. Insets: corresponding simulations.

**Table 1.** Simulated ([simu]) and experimentally measured ([exp]) figures of merit of the modal metasurfaces.

| | design | $l'=1$ | $l'=2$ | $l'=3$ |
|---|---|---|---|---|
| $\eta$ [simu] | continuous | 0.68 | 0.55 | 0.47 |
| $\eta$ [simu] | discrete | 0.66 | 0.53 | 0.45 |
| $\eta$ [exp] | discrete | 0.44 | 0.36 | 0.33 |
| $\rho_{l,0}^{\mathrm{opt}}$ [simu] | continuous | 1 | 1 | 1 |
| $\rho_{l,0}^{\mathrm{opt}}$ [simu] | discrete | 0.9990 | 0.9985 | 0.9981 |
| $T$ [exp] | discrete | 0.30 | 0.25 | 0.24 |

The continuous design refers to the idealized design given by Equations (5) and (6) while the discrete design refers to the actual design with 13 distinct meta-atoms. $\eta$ is the $\mathbf{c}_{-\sigma}$-polarized power fraction of the output beam, $\rho_{l,0}^{\mathrm{opt}}$ is the optimal power fraction of the targeted mode of the $\mathbf{c}_{-\sigma}$-polarized component (see Experimental Section) and T is the $\mathbf{c}_{-\sigma}$-polarized power transmittance.

expected to interact for the largest aspect ratios $L/W$ due to interdistances down to a few tens of nanometers, as shown in Figure S4g (Supporting Information). All these practical points, which are not accounted when designing the metasurfaces, make it difficult to develop a fully quantitative approach, although noticing that recent efforts in this direction have started.[15] Still, one can summarize a few figures of merit of the proposed approach, which are collected in **Table 1**.

As highlighted by the Table 1, only a fraction of the incident power is converted into the prescribed Laguerre–Gauss beam. At first, there is a fundamental reason inherent to the complex amplitude modulation scheme. This sets an upper limit for the parameter $\eta$ (the $\mathbf{c}_{-\sigma}$-polarized power fraction of the output beam), see the first line of Table 1, that corresponds to an optimal continuous design when all other sources of limitations than the space-varying retardance are discarded. Other sources of efficiency lowering have various origins, such as (i) residual absorption, (ii) the use of a piecewise design, (iii) nanofabrication errors, and (iv) Fresnel reflection. Drawbacks related to item (i) can be reduced by working with appropriate combination of the material and operating wavelength, as is the case here, see Figure S1d (Supporting Information) that highlights negligible absorption in the visible domain for wavelength >500 nm. The detrimental effects of item (ii) on $\eta$ have been evaluated numerically, see the second line of Table 1, which are of the order of a few percent. Experimentally, we find substantially smaller values, which could be explained by the item (iii) as mentioned in the preceding paragraph as well as diffractive losses inherent to discrete designs that involves structural discontinuities for the effective optical properties. An example of it can be found in the context of nonmodal optical vortex generation using dielectric metasurfaces having a discrete design of an azimuthal nature.[20] Finally, the item (iv) is expected to induce substantial reflection losses when using materials with high refractive index as is the case here, see Figure S1d (Supporting Information). A subtler effect from Fresnel reflection is related to the optical anisotropy of the metasurface which brings an additional space-variant modification of the polarization state of the light field that propagates through the material, which is not compensated by design in the present work. Still, we notice that anisotropic Fresnel reflection is not necessarily a drawback as it can be turned into a way to achieve pure ultrabroadband geometric phase reflective masks.[21] All these points allows understanding why the experimentally measured parameter $T$ (the $\mathbf{c}_{-\sigma}$-polarized power transmittance) is substantially smaller (by an amount of 35% on average for the three explored structures) than the experimentally measured parameter $\eta$, see Table 1. Of course, this also motivates for further improvements.

Finally, we note that the modal character of the metasurfaces is not questioned by the departure of the incident beam with respect to the reported continuous design that optimizes the output modal power, at least for $p = 0$. Indeed, it can be shown that when $w_{\mathrm{in}} \neq w_{\mathrm{design}}$ the device remains purely modal, though for an output beam waist

$$w_{\mathrm{out}} = w_{\mathrm{design}} \sqrt{\frac{2}{\left(1+|l|\right)\left(1+w_{\mathrm{design}}^2/w_{\mathrm{in}}^2\right)}} \tag{9}$$

Nevertheless, the parameter $\eta$ decreases from its maximal value when $w_{\mathrm{in}} \neq w_{\mathrm{design}}$ as shown from the simulations presented in **Figure 6**. We find that a 10% relative variation for the incident beam waist from the optimal operating conditions typically leads to 1% relative deviation for the parameter $\eta$. Moreover, in the incident beam impinges on the device with a spherical curvature—that is, if the metasurface is not placed in the focal plane of the incident fundamental Gaussian beam—a pure modal behavior still applies as a spherical lens does not alter the modal content of a beam. All this emphasizes the robust features of the proposed approach toward the development of user-friendly spin-orbit modal vortex plates.

## 4. Conclusion

Prospective developments of spin-orbit modal optical metasurfaces go beyond the particular example reported in this work. Indeed, complex amplitude shaping from single doubly-inhomogeneous anisotropic media—both in optical axis orientation and birefringence—can be deployed for arbitrary spatial patterns for intensity, phase, and polarization state which are

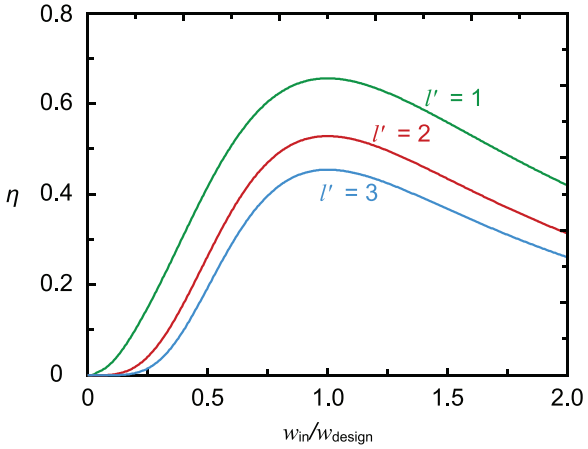


**Figure 6.** Deviation of the parameter $\eta$ from its maximal value for the design with $N = 13$, see second line of Table 1, as the incident beam waist $w_{\mathrm{in}}$ departs from the prescribed value $w_{\mathrm{design}}$ for $l' = 1, 2, 3$.

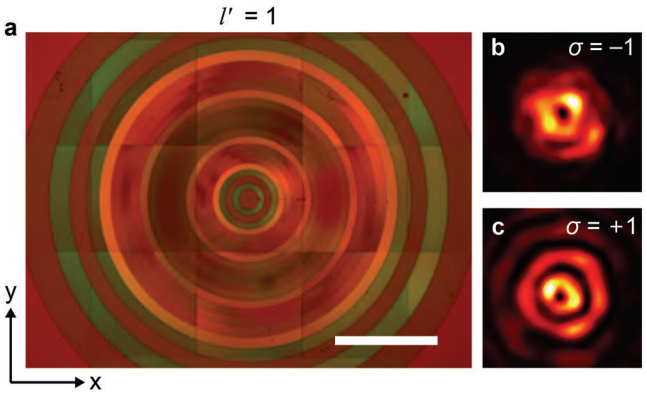


**Figure 7.** a) Reflection optical microscope image of a macroscopic modal metasurface with $l' = 1$, $R = 1.12$ mm and $w_{design} = 560$ µm. Scale bar: 500 µm. The panels b) and c) show the experimental intensity patterns of the circularly polarized component of the output field whose polarization state is orthogonal to the incident circularly polarized Gaussian (i.e., the $\mathbf{c}_{-\sigma}$-polarized component) beam for $\sigma = -1$ and $\sigma = +1$, respectively, at $z = 48$ mm.

ubiquitous to photonics technologies.[22] One of the future challenges are the capability to address the size issue since present metasurfaces remains in the realm of integrated devices. A proof of principle attempt is demonstrated in **Figure 7** for a clear aperture larger than 2 mm, using $R = 1.12$ mm and keeping $N = 13$ for the sake of illustration. This comes with technological challenges associated with the fabrication of metasurfaces with large dimensions. Such macroscopic drawback could be circumvented using ultrafast laser writing technology, however, dynamic phase management remains to date unsolved.[14] Another extension concerns the temporal domain, with the advent of reconfigurable modal spin-orbit devices, which has yet to be addressed.

## 5. Experimental Section

*Numerical Design*: The optical properties of the meta-atoms with different geometrical parameters were simulated by using the Lumerical FDTD software, whose monitor is depicted in Figure S1a (Supporting Information). The optical elements are composed of the $SiN_x$ meta-atoms which are sitting on a glass substrate. The period of the unit cell is $P = 430$ nm, the height of the $SiN_x$ meta-atoms is $H = 1400$ nm and the orientation angle for all $SiN_x$ meta-atoms is $\psi = 0$. Under normal illumination by a circularly polarized monochromatic plane wave at wavelength $\lambda = 633$ nm, the magnitude and phase of the transmission coefficient $t_{-\sigma}$ for the output with opposite circular polarization are calculated by scanning the length $L$ and width $W$ of the meta-atoms, see Figure 3a,b respectively.

*Nanofabrication*: The fabrication process starts with the deposition of a 1400 nm thick silicon nitride thin film on a doubled-polished fused silica substrate by using inductively coupled plasma (ICP) plasma-enhanced chemical vapor deposition (PECVD) process. Then, a 130 nm thick poly-methyl methacrylate (PMMA) e-beam resist layer was spin-coated onto the substrate and baked at the temperature of 180 °C for 3 min. Then, a 70 nm thick charge-dissipation layer is spin-coated on the top of the PMMA layer. Next, the sample was exposed by using electron-beam lithography (EBL) to write the patterns of metasurface. After that, the charge-dissipation layer was removed by using DI water for 1 min, and the PMMA layer was developed with a mixture of methyl isobutyl ketone and isopropyl alcohol (MIBK: IPA) for 2 min. Then, a 20 nm thick chromium (Cr) layer as a hard mask was deposited on the patterned PMMA layer by using electron beam evaporation and the Cr patterns appeared after the lift-off process. The sample with patterned Cr hard mask layer was etched through the 1400 nm thick $SiN_x$ thin film via the ICP etching process with the mixture of $CHF_3$ and $O_2$ gases. Finally, the metasurfaces were obtained by removing the residual Cr layer with chromium etchant solution. See Figure S3 (Supporting Information) for a schematic illustration of the different fabrication steps of the metasurfaces.

*Structural Characterization*: Optical microscope imaging of the fabricated metasurfaces shown in Figures 2b and 7a and Figure S8a–c (Supporting Information) have been recorded using Zeiss Microscope (Axio Observer) in the reflection mode using a mercury vapor short-arc lamp source and a 10× microscope objective. The SEM images displayed in Figures S4 and S8d–i (Supporting Information) have been recorded by using the Merlin FE-SEM (Zeiss) with 5 kV voltage and 100 pA current. It was noticed that a ≈15 nm thick Cr film was deposited on the top of the $SiN_x$ metasurface as the charge-dissipation layer for SEM imaging while the Cr film was removed before beam shaping experiments by immersing the metasurface into the chromium etchant solution.

*Beam Propagation*: Beam propagation from the metasurface to a distance $z$ is numerically evaluated by fast Fourier transform. Namely,

$$E(x,y,z) = F^{-1}\left[F\left[E(x,y,0)\right]\exp\left[ik_z z\right]\right] \tag{10}$$

where $F$ and $F^{-1}$ refer to fast Fourier and inverse fast Fourier transforms, $k_z = \left(k^2 - k_x^2 - k_y^2\right)^{1/2}$ with $\mathbf{k} = k_x\mathbf{x} + k_y\mathbf{y} + k_z\mathbf{z}$ being the wavevector, and the field $E(x, y, 0)$ is taken as the $\mathbf{c}_{-\sigma}$-polarized component at the output of the metasurface, hence $E(x,y,0) = E_0 \exp\left[-\left(x^2+y^2\right)/w_{in}^2\right]\left|t_{-\sigma}(x,y)\right|$ according to the piecewise design with 25 concentric zones as described in the text and detailed in Table S2 (Supporting Information).

*Modal Decomposition*: The decomposition of the output field emerging from the optical element onto the Laguerre–Gauss basis allows defining the power fraction $\rho_{l,p}$ of each of the constituting modes $(l, p)$ given by Equation (1). Namely,

$$\rho_{l,p}(w) = \left| \frac{\int_0^\infty \left(\mathbf{E}_{out}\cdot\mathbf{c}_{-\sigma}^*\right) E_{l,p}^*(w)\, rdr}{\sqrt{\int_0^\infty \left|\mathbf{E}_{out}\cdot\mathbf{c}_{-\sigma}^*\right|^2 rdr \int_0^\infty \left|E_{l,p}(w)\right|^2 rdr}} \right|^2 \tag{11}$$

where the asterisk denotes complex conjugation and the dependence of the field on spatial coordinates has been omitted. The dependence on $w$ highlights the fact that the decomposition is not unique. Consequently, targeting a given mode, the optimal modality is defined as

$$\rho_{l,p}^{opt} = \max_w \left|\rho_{l,p}(w)\right|^2 \tag{12}$$

[1] W. W. Rigrod, *Appl. Phys. Lett.* **1963**, *2*, 51.
[2] O. Bryngdahl, *J. Opt. Soc. Am.* **1973**, *63*, 1098.
[3] J. M. Vaughan, D. V. Willetts, *Opt. Commun.* **1979**, *30*, 263.
[4] P. Coullet, L. Gil, F. Rocca, *Opt. Commun.* **1989**, *73*, 403.
[5] L. Allen, M. W. Beijersbergen, R. J. C. Spreeuw, J. P. Woerdman, *Phys. Rev. A* **1992**, *45*, 8185.
[6] A. E. Siegman, *Lasers*, University Science Books, CA, USA **1986**.
[7] A. Forbes, A. Dudley, M. McLaren, *Adv. Opt. Photonics* **2016**, *8*, 200.
[8] B. Sephton, A. Dudley, A. Forbes, *Appl. Opt.* **2016**, *55*, 7830.
[9] S. N. Khonina, V. V. Kotlyar, R. V. Skidanov, V. A. Soifer, P. Laakkonen, J. Turunen, *Opt. Commun.* **2000**, *175*, 301.
[10] G. Ruffato, M. Massari, F. Romanato, *Opt. Lett.* **2014**, *39*, 5094.
[11] P. Chen, B.-Y. Wei, W. Ji, S.-J. Ge, W. Hu, F. Xu, V. Chigrinov, Y.-Q. Lu, *Photonics Res.* **2015**, *3*, 133.
[12] M. Rafayelyan, E. Brasselet, *Opt. Lett.* **2017**, *42*, 1966.
[13] M. Rafayelyan, T. Gertus, E. Brasselet, *Appl. Phys. Lett.* **2017**, *110*, 261108.
[14] D. Coursault, E. Brasselet, *Nanophotonics* **2022**, *11*, 805.
[15] H. Mao, Y.-X. Ren, Y. Yu, Z. Yu, X. Sun, S. Zhang, K. K. Wong, *Photonics Res.* **2021**, *9*, 1689.
[16] M. Piccardo, A. Ambrosio, *Nanophotonics* **2021**, *10*, 727.
[17] B. Radhakrishna, G. Kadiri, G. Raghavan, *J. Opt. Soc. Am. B* **2021**, *38*, 1909.
[18] H. Ahmed, H. Kim, Y. Zhang, Y. Intaravanne, J. Jang, J. Rho, S. Q. Chen, X. Z. Chen, *Nanophotonics* **2022**, *11*, 941.
[19] A. Y. Bekshaev, M. S. Soskin, M. V. Vasnetsov, *Opt. Commun.* **2004**, *241*, 237.
[20] M. G. Nassiri, G. Seniutinas, C. David, S. Juodkazis, E. Brasselet, *Appl. Phys. Lett.* **2021**, *118*, 201104.
[21] M. G. Nassiri, E. Brasselet, *Phys. Rev. A* **2019**, *99*, 013836.
[22] M. Piccardo, V. Ginis, A. Forbes, S. Mahler, A. A. Friesem, N. Davidson, H. Ren, A. H. Dorrah, F. Capasso, F. T. Dullo, B. S. Ahluwalia, A. Ambrosio, S. Gigan, N. Treps, M. Hiekkamäki, R. Fickler, M. Kues, D. Moss, R. Morandotti, J. Riemensberger, T. J. Kippenberg, J. Faist, G. Scalari, N. Picqué, T. W. Hänsch, G. Cerullo, C. Manzoni, L. A. Lugiato, M. Brambilla, L. Columbo, et al., *J. Opt.* **2021**, *24*, 013001.